Optics Letters

Constructing multifunctional wave plates with stereo-metastructure arrays

Sijia Sun,[1] Yajun Gao,[1] Xiang Xiong,[1,2] Ruwen Peng,[1,3] and Mu Wang[1,4]

[1]National Laboratory of Solid State Microstructures, School of Physics, and Collaborative Innovation Center of Advanced Microstructures, Nanjing University, Nanjing 210093, China
[2]e-mail: xiang@nju.edu.cn
[3]e-mail: rwpeng@nju.edu.cn
[4]e-mail: muwang@nju.edu.cn

Received 4 February 2019; revised 28 February 2019; accepted 5 March 2019; posted 5 March 2019 (Doc. ID 359551); published 28 March 2019

Driven by the development of nanophotonics and integrated optics, manipulating polarization of light with metastructures has been extensively studied in recent decades. So far there is still a high demand for more efficient ways to control the polarization state of light with extraordinary performance. In this Letter, we report on constructing multifunctional wave plates with stereo-metastructure arrays (SMAs) by two-photon absorption polymerization. In one frequency range, the SMA can turn the polarization direction of incident linearly polarized (LP) light to its orthogonal direction, acting as a half-wave plate (HWP). In the other frequency range, it converts the LP incident light to circularly polarized (CP) light, acting as a quarter-wave plate (QWP). Such a multifunctional element is expected to possess an energy efficiency as high as 75%. By encoding SMAs with different rotation angles at different spatial areas, we show that SMAs can be applied in imaging and sensing, where the focal-plane-array (FPA) imaging demonstrates patterned contrast following different structural distribution.

https://doi.org/10.1364/OL.44.001758

Polarization is an important feature of electromagnetic waves, and conversions between different polarization states are indispensable for modern electromagnetic and photonic applications. Conventionally, polarization can be manipulated with a birefringent crystal sheet, which accumulates the required phase difference between two orthogonally polarized wave components (o-ray and e-ray) [1]. To achieve a certain phase difference, the birefringence-based wave plates are usually bulky, which do not meet the requirements of nanophotonics and integrated optics [2]. In the past decade, different metastructures have been developed to manipulate the polarization states in microwave [3–5], terahertz [6–12], infrared [13–22], and visible [23–28] regimes. So far, a large fraction of metastructures is based on the induced electromagnetic resonances [8,18]. However, the underlying resonance may lead to narrow working frequency band. One way to broaden the working frequency range is to superimpose different resonant modes in a unit cell [12,27]. The other way to broaden the bandwidth is to use conjugation compensation in the metal-insulator-metal system [14]. By integrating metallic metastructures and dielectric interlayer, the intrinsic dispersion generated by the resonance of metallic structure can be perfectly canceled out by the interlayer-thickness-sensitive dispersion of the dielectric interlayer, so the dispersion-free optical functionalities can be realized in a very restricted space.

The multifunction design is another approach to integrating the element. Realizing different functionalities with one single element may miniaturize the element size, and the fabrication process can be simplified as well. However, due to the uncontrollable electro-magnetic coupling effect between different parts of the element, the design of the multifunctional metastructures is difficult [3,29]. In this Letter, by two-photon absorption (TPA) polymerization, we demonstrate the multifunctional wave plates with T-shaped structure (TSS) and X-shaped structure (XSS). Both of these stereo-metastructure arrays (SMAs) consist of the elementary standing brick-shaped structures (BSSs). Spectral measurements show that for the TSS design, a quarter-wave plate (QWP) functions in the lower frequency range, whereas it works as a half-wave plate (HWP) in the higher frequency range. XSS works as an HWP in the lower frequency range while it functions as a QWP in the higher frequency range. Further, we fabricate a pattern with XSS array and characterize it with focal-plane-array (FPA) spectroscopy. The FPA images collected in different frequency ranges confirm the optical multifunctionality of the SMA design.

The stereo-metastructure is fabricated by two-photon absorption setup (Photonic Professional, Nanoscribe GmbH). The writing area without stitching is $300 \times 300\ \mu m^2$, which is limited by the piezo stage range. Details of the TPA technique can be seen in [30]. During the fabrication, the focus point of the femtosecond laser scans in space following a pre-designed three-dimensional (3D) pattern. The precursor at the focus point of the femtosecond laser is polymerized and solidified, while the unexposed photoresist can be removed in the developing process by propylene glycol monomethyl ether acetate (PGMEA, Sigma-Aldrich). In this way, a polymer skeleton of an SMA is fabricated. Then, we coat the polymer skeleton of the SMA and the upper surface of the glass substrate

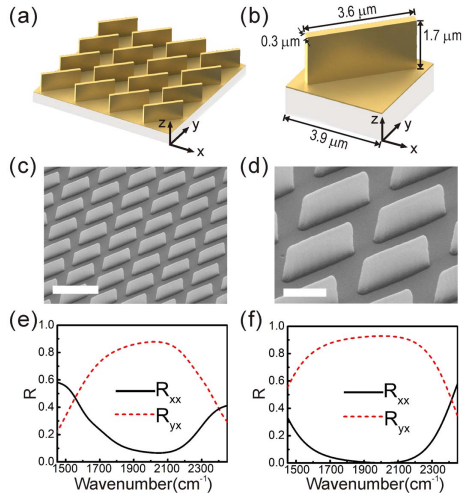

Fig. 1. (a) Schematic diagram of the BSS array. (b) The detailed topography of the BSS unit. (c) The SEM micrograph of the fabricated BSS array. The scale bar represents 5 μm. (d) The zoomed-in SEM micrograph of the BSS. The scale bar represents 2 μm. The measured (e) and simulated (f) reflections for different polarization arrangements.

with a gold layer 35 nm in thickness by magnetron sputtering. The morphology of the sample is observed with a scanning electron microscope (SEM, Zeiss Ultra 55).

Before constructing the TSS and XSS arrays, a standing BSS is designed as the elementary building block for the multifunctional wave plates. A sketch of the BSS array and the unit cell of the building blocks are shown in Figs. 1(a) and 1(b), respectively. As shown in Figs. 1(a) and 1(b) the coordinate system is so set that the BSSs stand along the direction of 45° which is the diagonal direction of the unit. An array of such units is arranged in a simple square lattice, and the unit cell is reproduced in x- and y-directions with the same lattice constant. The SEM micrographs of the fabricated BSS array are presented in Figs. 1(c) and 1(d). A Fourier transform infrared (FTIR) spectrometer (Bruker Vertex 70 v) associated with an infrared microscope with an FPA detector (Bruker Hyperion 3000) is employed for optical characterization. Two ZnSe wire grid polarizers with the same transmittance and polarization characteristics are used as the polarizer and analyzer for optical measurement. The measured results are shown in Fig. 1(e) where R_{ij} represents the reflection intensity of the i component of the reflected light induced by j-polarized incidence ($i = x$, y; $j = x$). Figure 1(e) indicates that over 70% (90% is achieved at 2000 cm^{-1}) of the x-polarized incident light is turned to the y-polarized reflected light in the frequency range of 1700–2200 cm^{-1}. In this frequency range, the BSS array serves as a broadband HWP which can change the polarization direction of linearly polarized (LP) light to its orthogonal direction. The optical properties of BSSs have been calculated based on finite difference time domain (FDTD) method [19]. As shown in Fig. 1(f), FDTD calculation results show a good agreement with the measurements. It can be seen that the measured working frequency range is narrower than that in the simulation. This is because during the fabrication process, the polymer structures fabricated by the TPA process tend to shrink and collapse. A 5%-10% shrinkage rate may cause an obvious narrowing of the working frequency band. The surface wrinkling may also cause the inconsistency between experiment and simulation [31]. Comparing with our previous design (an assembly of standing metallic L-shaped structures) [19], the BSS array can play the role of broadband wave plates with smaller space volume, which is more favorable in designing integrated optical element.

Compared with two-dimensional (2D) metastructures, stereo-metastructures provide more degrees of freedom to tune their optical properties [32,33]. Here we construct a T-shaped structure by BSS with different heights. Figures 2(a) and 2(b) illustrate the designing of the TSS array and the unit cell. As shown in Figs. 2(a) and 2(b), the TSS unit cell consists of two discontinuous BSSs: one is taller than the other, and they are perpendicular to each other. The end of the lower BSS points to the center of the taller one. In the coordinates shown in Figs. 2(a) and 2(b), the x- and y-axis are along the diagonal directions of the unit cell. The taller BSS lies along 135°-direction, and the lower one lies along 45°-direction. The TSS unit is periodically repeated along 45°- and 135°-directions to form an array. Figure 2(c) illustrates the oblique SEM view of the TSS sample. The enlarged micrograph in Fig. 2(d) shows more details of the fabricated structure. FTIR spectroscopy measurements are shown in Fig. 2(e). The measured reflections show that when the incident light is polarized along the x-direction, the reflected x-component R_{xx} and y-component R_{yx} of light are almost identical in the lower frequency range of 1500–1950 cm^{-1}. The measured total reflection intensity ($R_{xx} + R_{yx}$) is more than 75%. From 1950 cm^{-1} to 2100 cm^{-1} the x-direction component R_{xx} decreases and the y-direction component R_{yx} increases quickly. In the frequency range of 2100–2300 cm^{-1}, R_{xx} is suppressed, and most of the incident power (more than 70%) is transferred to R_{yx}. The retrieved phase difference between R_{xx} and R_{yx} [19] is maintained at about 90° in the lower frequency range. Figure 2(f) shows that

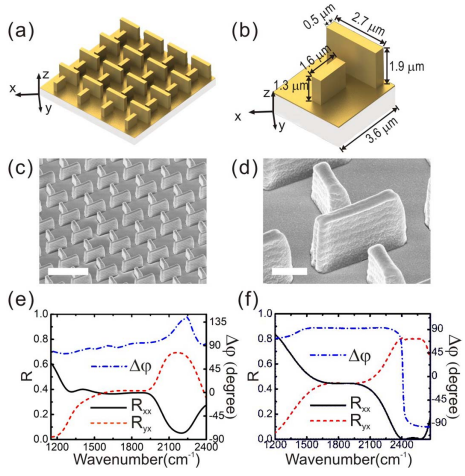

Fig. 2. (a) Schematic diagram of the TSS array. (b) The detailed topography of the TSS unit cell. The gap width between the shorter and taller BSSs is 0.76 μm, and the thickness of the metal film is 35 nm. (c) The SEM micrograph of the fabricated TSS array, the scale bar represents 5 μm. (d) The zoomed-in imaging of the TSS array; the scale bar represents 1 μm. (e) The measured reflections and the retrieved phase difference of the TSS array for different polarization arrangements. (f) The calculated reflections and the phase difference for different polarization arrangements.

the simulation results are consistent with the experimental ones, except for the phase difference in the higher frequency. This is because the retrieved method becomes inaccuracy when the intensity of R_{xx} is close to zero. The amplitude and the phase difference indicate that in the lower frequency range, the TSS array has converted the LP light to circularly polarized (CP) light, which functions as a broadband QWP. Meanwhile, in the higher frequency range, the TSS array converts the polarization direction of the LP light to the orthogonal direction and works as a broadband HWP. The different optical functions are attributed to different modes at lower and higher frequencies. The broadband property comes from the 3D metallic BSS and the flat metallic upper surface which form a phase-conjugation system [14]. The optical response of the stereo-metastructure is sensitive to the incident angle. The incoming light alignment regarding the structure orientation is important.

The idea to design multifunctional stereo-metastructures by combining different 3D building blocks can be extended. By assembling BSS elements in a different way, we construct another multifunctional XSS wave plate. The designing of the array and the unit cell of the XSSs are illustrated in Figs. 3(a) and 3(b), where the XSS unit cell consists of a higher BSS and two identical lower BSSs. In the coordinate shown in Figs. 3(a) and 3(b), the higher BSS lies along 135°-direction while the two shorter BSSs lie along 45°-direction. The two lower BSSs are located on both sides of the taller BSS and perpendicularly point to the middle of the taller BSS. Figures 3(c) and 3(d) illustrate the top-view and the enlarged side-view SEM micrograph of the fabricated structure. The FTIR measurement of the XSS array is presented in Fig. 3(e). The reflection intensity of x- and y-components indicates that in the lower frequency range (1400–1900 cm^{-1}) the x-component of light is suppressed and most of the x-polarized incident power (more than 80%) is converted to y-polarized reflection. In the higher frequency range (2100–2300 cm^{-1}), the amplitudes of x- and y-components are almost identical, and the measured total reflection intensity ($R_{xx} + R_{yx}$) is about 70%. The retrieved phase difference between x- and y-components is almost 90° in the higher frequency range which means the XSS array plays a role of QWP. The simulated optical properties of XSS array are shown in Fig. 3(f). It can be seen that the simulation is in good agreement with the experimental results. In the lower frequency, the XSS array converts the polarization direction of LP light to the orthogonal direction and functions as an HWP. In the higher frequency, the XSS array has converted polarization from LP to CP which functions as a QWP. The theoretical analysis of the polarization conversion and the dispersion-free property based on the phase-conjugation method can be found in [14,19].

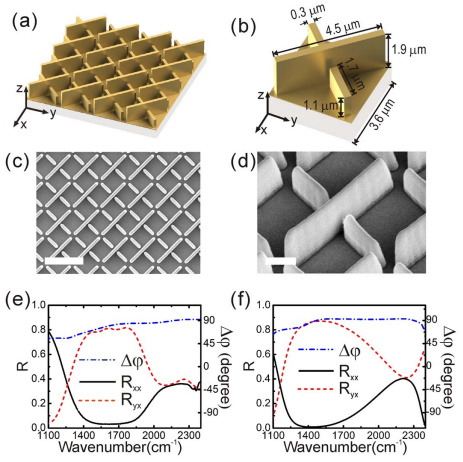

Fig. 3. (a) Schematic diagram of the XSS array. (b) The detailed topography of the XSS unit cell. (c) The top-view SEM micrograph of the fabricated XSS array, the scale bar represents 5 μm. The gap width between the taller and shorter BSSs is 0.27 μm. (d) The zoomed-in micrograph of the fabricated XSS unit; the scale bar represents 1 μm. (e) The measured reflections and the retrieved phase difference of the XSS array for different polarization arrangements. (f) The calculated reflection and phase difference of the XSS array for different polarization arrangements.

Now we show that the role of the multifunctional wave plate of XSSs can be characterized by FPA spectroscopy equipped with a polarizer and an analyzer. The top-view SEM micrograph of the patterned sample is shown in Fig. 4(a). As shown in the insets, the unit cells XSS_1, XSS_2, XSS_3, and XSS_4 have the same geometrical structure but are rotated clockwise by 0°, 45°, 90°, and 135°, respectively. The $U-V$ coordinate system is created and fixed on the substrate, and the $x-y$ coordinate system is rotated with XSS units. In the FPA measurement setup, θ_{inc} (θ_{ref}) represents the angle between the polarization directions of the polarizer (analyzer) and the U-axis. The corresponding measured FPA micrographs are shown in Figs. 4(b)–4(g).

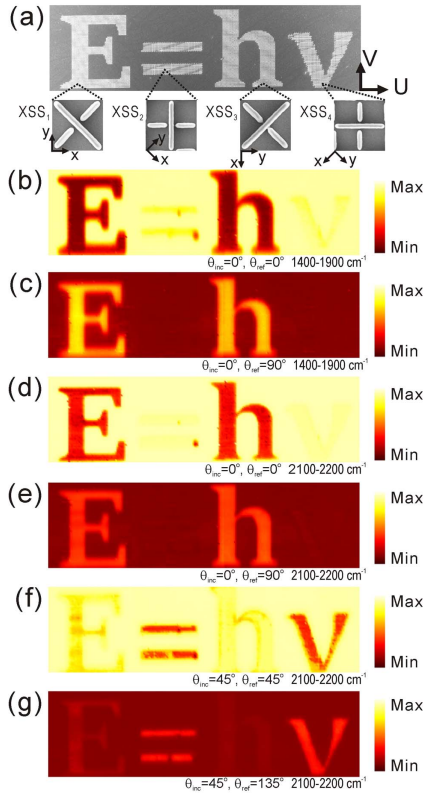

Fig. 4. (a) SEM micrograph of the patterned sample. The size of the whole sample is 220 μm × 840 μm. The insets show the unit cells of the four characters. (b)–(g) FPA images integrated in lower and higher frequency ranges for different polarization/analyzation arrangements.

In Figs. 4(b)–4(e), the incident light is polarized along U-axis ($\theta_{inc} = 0°$). In the lower frequency range of 1400–1900 cm^{-1}, the XSS functions as an HWP. For XSS_1 and XSS_3, the incident light is equivalently polarized along x- and y-direction, respectively. In this case, XSS_1 and XSS_3 can both convert the polarization direction of the LP light to its perpendicular direction. In the FPA image shown in Fig. 4(b), "E" and "h" show minimum brightness because the reflected light is blocked by the analyzer with $\theta_{ref} = 0°$. In Fig. 4(c), "E" and "h" show maximum brightness, because the reflected light can pass through the analyzer with $\theta_{ref} = 90°$. In the higher frequency range of 2100–2200 cm^{-1}, XSS functions as a QWP. XSS_1 and XSS_3 can convert the polarization of the incident light from LP to CP. In the measured FPA images of Figs. 4(d) and 4(e), "E" and "h" show medium brightness because partial energy of the reflected CP light can pass through the linear analyzers with $\theta_{ref} = 0°$ and $\theta_{ref} = 90°$.

The patterns "=" and "v" in Figs. 4(b) and 4(d) show the maximum brightness, while those in Figs. 4(c) and 4(e) show the minimum brightness. This is because for XSS_2 and XSS_4, the incident light is polarized along the symmetrical axes of the XSS unit. The polarization direction of the reflected light is unchanged. In this case, the reflected light can pass through the linear analyzers in Figs. 4(b) and 4(d), but is blocked by the linear analyzers in Figs. 4(c) and 4(e).

We then change the polarization direction of the incident light to $\theta_{inc} = 45°$. In the higher frequency range, XSS_2 and XSS_4 convert the polarization of light from LP to CP. Figures 4(f) and 4(g) show the FPA images collected in the frequency range of 2100–2200 cm^{-1}. Partial power of the reflected CP light can pass through the linear analyzers with $\theta_{ref} = 45°$ and $\theta_{ref} = 135°$. This is confirmed by the medium brightness of the patterns "=" and "v" in Figs. 4(f) and 4(g). The patterns "E" and "h" in Fig. 4(f) show the maximum brightness, while those in Fig. 4(g) show the minimum brightness. This is because for XSS_1 and XSS_3, the incident light is polarized along the symmetrical axes of the XSS unit. The polarization of reflected light is unchanged. The reflected light can pass through the linear analyzer with $\theta_{ref} = 45°$ in Fig. 4(f), but it is blocked by the linear analyzer with $\theta_{ref} = 135°$ in Fig. 4(g). The FPA spectroscopy confirms that the SMAs indeed play different roles of QWP and HWP in higher and lower frequency ranges, respectively.

In summary, we have demonstrated that with the same metastructure we can realize two broadband wave plates with different functionalities at different frequency ranges. This work provides a new approach to manipulating the polarization states of light with stereo-metastructures. By using multifunctional wave plates, dual-broadband LP, LCP, and RCP lights can be obtained flexibly for spectral analysis. The frequency-dependent polarization modulation in the mid-infrared wavelength region may also find applications in multiband polarization imaging and sensing [34].

Funding. National Key R&D Program of China (2017YFA0303702); National Natural Science Foundation of China (NSFC) (11574141, 11674155, 11634005, 11621091); Natural Science Foundation of Jiangsu Province (BK20160065, BRA2016350).

REFERENCES

1. M. Born, E. Wolf, and A. B. Bhatia, *Principles of Optics: Electromagnetic Theory of Propagation, Interference and Diffraction of Light* (Cambridge University, 1999).
2. R. G. Hunsperger, *Integrated Optics Theory and Technology*, 3rd ed. (Springer-Verlag, 1991).
3. P. C. Wu, W. Zhu, Z. X. Shen, P. H. J. Chong, W. Ser, D. P. Tsai, and A.-Q. Liu, Adv. Opt. Mater. **5**, 1600938 (2017).
4. L. Chen, X. Ke, H. Guo, J. Li, X. Li, and L. Zhou, Sci. Rep. **8**, 1051 (2018).
5. J. Xu, R. Li, J. Qin, S. Wang, and T. Han, Opt. Express **26**, 20913 (2018).
6. S. Liu, T. J. Cui, Q. Xu, D. Bao, L. Du, X. Wan, W. X. Tang, C. Ouyang, X. Y. Zhou, H. Yuan, H. F. Ma, W. X. Jiang, J. Han, W. Zhang, and Q. Cheng, Light: Sci. Appl. **5**, e16076 (2016).
7. W. Mo, X. Wei, K. Wang, Y. Li, and J. Liu, Opt. Express **24**, 13621 (2016).
8. D. Wang, Y. Gu, Y. Gong, C.-W. Qiu, and M. Hong, Opt. Express **23**, 11114 (2015).
9. X. Zhao, J. Schalch, J. Zhang, H. R. Seren, G. Duan, R. D. Averitt, and X. Zhang, Optica **5**, 303 (2018).
10. J. Zi, Q. Xu, Q. Wang, C. Tian, Y. Li, X. Zhang, J. Han, and W. Zhang, Appl. Phys. Lett. **113**, 101104 (2018).
11. L. Cong, Y. K. Srivastava, H. Zhang, X. Zhang, J. Han, and R. Singh, Light: Sci. Appl. **7**, 788 (2018).
12. R.-H. Fan, Y. Zhou, X.-P. Ren, R.-W. Peng, S.-C. Jiang, D.-H. Xu, X. Xiong, X.-R. Huang, and M. Wang, Adv. Mater. **27**, 1201 (2015).
13. F. Ding, Z. Wang, S. He, V. M. Shalaev, and A. V. Kildishev, ACS Nano **9**, 4111 (2015).
14. S.-C. Jiang, X. Xiong, Y.-S. Hu, Y.-H. Hu, G.-B. Ma, R.-W. Peng, C. Sun, and M. Wang, Phys. Rev. X **4**, 021026 (2014).
15. S.-C. Jiang, X. Xiong, P. Sarriugarte, S.-W. Jiang, X.-B. Yin, Y. Wang, R.-W. Peng, D. Wu, R. Hillenbrand, X. Zhang, and M. Wang, Phys. Rev. B **88**, 161104(R) (2013).
16. T. Li, L. Huang, J. Liu, Y. Wang, and T. Zentgraf, Opt. Express **25**, 4216 (2017).
17. A. Shaltout, J. Liu, A. Kildishev, and V. Shalaev, Optica **2**, 860 (2015).
18. C. Wu, N. Arju, G. Kelp, J. A. Fan, J. Dominguez, E. Gonzales, E. Tutuc, I. Brener, and G. Shvets, Nat. Commun. **5**, 3892 (2014).
19. X. Xiong, Y.-S. Hu, S.-C. Jiang, Y.-H. Hu, R.-H. Fan, G.-B. Ma, D.-J. Shu, R.-W. Peng, and M. Wang, Appl. Phys. Lett. **105**, 201105 (2014).
20. Y. Yang, W. Wang, P. Moitra, I. I. Kravchenko, D. P. Briggs, and J. Valentine, Nano Lett. **14**, 1394 (2014).
21. N. Yu, F. Aieta, P. Genevet, M. A. Kats, Z. Gaburro, and F. Capasso, Nano Lett. **12**, 6328 (2012).
22. Z. Wang, H. Jia, K. Yao, W. Cai, H. Chen, and Y. Liu, ACS Photon. **3**, 2096 (2016).
23. D. Lee, S. Y. Han, Y. Jeong, D. M. Nguyen, G. Yoon, J. Mun, J. Chae, J. H. Lee, J. G. Ok, G. Y. Jung, H. J. Park, K. Kim, and J. Rho, Sci. Rep. **8**, 12393 (2018).
24. X. Ni, A. V. Kildishev, and V. M. Shalaev, Nat. Commun. **4**, 2807 (2013).
25. F. Qin, L. Ding, L. Zhang, F. Monticone, C. C. Chum, J. Deng, S. Mei, Y. Li, J. Teng, M. Hong, S. Zhang, A. Alù, and C.-W. Qiu, Sci. Adv. **2**, e1501168 (2016).
26. P. C. Wu, W.-Y. Tsai, W. T. Chen, Y.-W. Huang, T.-Y. Chen, J.-W. Chen, C. Y. Liao, C. H. Chu, G. Sun, and D. P. Tsai, Nano Lett. **17**, 445 (2017).
27. Y. Zhao and A. Alù, Nano Lett. **13**, 1086 (2013).
28. L. H. Nicholls, F. J. Rodríguez-Fortuño, M. E. Nasir, R. M. Córdova-Castro, N. Olivier, G. A. Wurtz, and A. V. Zayats, Nat. Photonics **11**, 628 (2017).
29. H. Cheng, X. Wei, P. Yu, Z. Li, Z. Liu, J. Li, S. Chen, and J. Tian, Appl. Phys. Lett. **110**, 171903 (2017).
30. S. Kawata, H. B. Sun, T. Tanaka, and K. Takada, Nature **412**, 697 (2001).
31. J. Purtov, A. Verch, P. Rogin, and R. Hensel, Microelectron. Eng. **194**, 45 (2018).
32. N. Liu, H. Liu, S. Zhu, and H. Giessen, Nat. Photonics **3**, 157 (2009).
33. Y. Zhao, J. Shi, L. Sun, X. Li, and A. Alù, Adv. Mater. **26**, 1439 (2014).
34. Y. Zhao, Q. Peng, C. Yi, and S. G. Kong, J. Sens. **2016**, 5985673 (2016).